Journal of Materials Chemistry A

ROYAL SOCIETY OF CHEMISTRY

PAPER

View Article Online
View Journal | View Issue



Cite this: J. Mater. Chem. A, 2024, 12, 5319

# Electrosynthesis of ruthenium nanocluster incorporated nickel diselenide for efficient overall water splitting†

Vipin Yadav,[a] Megha,[b] Prasenjit Sen *[b] and M. M. Shaijumon *[a]

Design of effective catalyst activation strategies that enable efficient electrocatalytic activity towards overall water splitting is necessary for the development of clean energy conversion technologies. Incorporation of metal nanoclusters effectively increases the active site exposure leading to enhanced electrocatalytic activity. Here, we present an energy-efficient and scalable single-step approach for the electrosynthesis of ruthenium nanocluster decorated nickel diselenide catalysts for high-performance and stable alkaline water splitting application. The catalyst exhibits exceptional bifunctional activity for both hydrogen and oxygen evolution, and we demonstrate remarkable full-cell performance with a cell potential of 1.45 V to deliver a current density of 10 mA $cm^{-2}$, along with impressive long-term stability over 400 h. Density functional theory (DFT) calculations are carried out, which demonstrate that the ruthenium nanocluster decoration facilitates the exothermic dissociation of water into H and OH species, while also optimizing the adsorption energies of $H^+$ and $OH^-$ when compared to bare $NiSe_2$. The present approach could be extended to a variety of catalytically active materials that would potentially be of interest for alkaline water-splitting applications.

Received 13th November 2023
Accepted 20th January 2024

DOI: 10.1039/d3ta06988e

rsc.li/materials-a



## Introduction

Hydrogen is considered as a promising energy carrier to replace the existing energy infrastructure, owing to its high gravimetric energy density (120 kJ $kg^{-1}$) and zero carbon emission features.[1,2] There are several methods for hydrogen production, based on the applied energy sources, such as high-temperature thermolysis, coal refining, electrocatalysis, photocatalysis, *etc.*[3–8] The electrochemical water cycle, which involves electrolysis of water for $H_2$ generation and subsequent utilization in fuel cells, is a significant approach towards a sustainable energy future. The energy conversion process involves two half-cell reactions, namely, the hydrogen evolution reaction (HER) happening at the cathode side, and the oxygen evolution reaction (OER) happening at the anode side.[9–12] Owing to the multistep reaction processes in alkaline media, the HER and OER suffer from high activation barriers, resulting in large overpotentials leading to the slow kinetics of water electrolysis.[13,14] Noble metal (Pt, Ir)-based electrocatalysts are currently regarded as the most active materials for the HER and OER. However, their high cost, limited availability, and poor stability hinder their large-scale applications.[15–17] Therefore it is highly essential to develop cost-effective, highly active, and highly stable commercial bifunctional electrocatalysts for overall water splitting.[18,19]

Currently, transition metal compounds including chalcogenides, oxides, hydroxides, carbides, phosphides, *etc.*, are studied as potential candidates for HER and OER activity towards water splitting.[20–26] Recently, transition metal selenides have gained much more attention because of their d-orbital configuration and better conductivity.[27–30] However, their electrochemical activity is still far from that of the benchmark catalysts because of their high adsorption energy, low number of electrochemically active sites, *etc.* In this context, several approaches such as forming heterostructures, creating defects, doping with other elements, strain modulation, *etc.*, are adopted to improve the overall activity of such catalysts.[31–35] Most importantly it is essential to improve the water dissociation ability to achieve enhanced alkaline HER activity.[36] Incorporation of another component, such as a sub-nanometer-sized metal or metal oxide cluster with strong water dissociation ability is an effective strategy for hydrogen production because of its strong quantum confinement effects.[37,38] Sub-nanometer metal nanocluster decoration effectively increases the active site exposure leading to enhanced electrocatalytic activity for overall water splitting.[39–42] There have been efforts devoted to developing non-platinum-based bifunctional electrocatalysts for water splitting. Ruthenium, belonging to the class of noble

[a]School of Physics, Indian Institute of Science Education and Research Thiruvananthapuram, Maruthamala PO, Vithura, Kerala, 695551, India. E-mail: shaiju@iisertvm.ac.in

[b]Harish-Chandra Research Institute, HBNI, Chhatnag Road, Jhunsi, Allahabad, 211019, India

† Electronic supplementary information (ESI) available. See DOI: https://doi.org/10.1039/d3ta06988e

metal elements, exhibits similar metal–hydrogen-bond strength of ~65 kcal $mol^{-1}$ activity to that of platinum and has a much lower price (~4% of platinum).[43,44] Ruthenium nanoclusters were shown to exhibit good ability for water dissociation by shifting the d-band center closer to the Fermi level, which is an important parameter for efficient alkaline water splitting.[45] Ruthenium nanocluster decoration over nickel diselenide following a two-step process of hydrothermal and selenization methods has been reported to lead to enhanced electrocatalytic water splitting in alkaline media.[46] However, the reported synthesis method involves multistep processes and high-temperature requirements, posing severe concerns toward practical implementation. Pu *et al.*, reported the electrodeposition of nickel diselenide nanoparticles over titanium foil for overall water-splitting application.[47] Ru-nanocluster growth on $NiSe_2$ over conducting substrates such as nickel foam (NF) or carbon material *via* a single-step process would enable high metal utilization and improved electronic conductivity, resulting in efficient catalytic activity towards overall water splitting.

Herein, we demonstrate an energy-efficient and scalable single-step approach for the electrosynthesis of ruthenium nanocluster decorated nickel diselenide catalysts for high-performance and stable alkaline water splitting application. We optimize catalyst synthesis, and the sample with 50 mmol Ru (50-Ru–$NiSe_2$) is shown to exhibit excellent bifunctional electrocatalytic activity with the lowest overpotential of 13 mV at a current density of 10 mA $cm^{-2}$ for the HER and 260 mV at a current density of 30 mA $cm^{-2}$ for the OER. We further demonstrate remarkable full-cell performance with a cell potential of 1.45 V to deliver a current density of 10 mA $cm^{-2}$, along with impressive long-term stability over 400 h. Density functional theory (DFT) calculations are carried out, which demonstrate that the ruthenium nanocluster decoration facilitates the exothermic dissociation of water into H and OH species, while also optimizing the adsorption energies of $H^+$ and $OH^-$ when compared to that of bare $NiSe_2$.

# Experimental section

### Materials and reagents

Nickel acetate tetrahydrate ($Ni(CH_3COOH)_2 \cdot 4H_2O$, 98%), selenium dioxide ($SeO_2$, 99.8%), ruthenium(III) chloride hydrate ($RuCl_3 \cdot xH_2O$, 99.98%), nickel foam (NF, 1.6 mm thickness), hydrochloric acid (HCl, 37%), potassium hydroxide pellets (KOH, 99.95%), platinum over carbon (20 wt% Pt/C), and iridium oxide ($IrO_2$, 99.9%) were purchased from Sigma-Aldrich. High-purity Milli-Q water was used for preparing the samples.

### Synthesis of Ru–$NiSe_2$

A piece of NF (0.5 cm × 1 cm) was initially treated with HCl for 10 min under sonication and then washed with DI water followed by drying at 60 °C overnight. For electrodeposition, we used a typical steady-state three-electrode setup in which HCl pretreated NF is used as the working electrode, a platinum coil is used as the counter electrode, and silver/silver chloride (Ag/AgCl) is used as the reference electrode. A constant potential of −1 V *vs.* Ag/AgCl is applied for 10 min at the working electrode for electrodeposition. First, we synthesized nickel diselenide ($NiSe_2$) using an electrolyte of 65 mmol of $Ni(CH_3COOH)_2 \cdot 4H_2O$, and 35 mmol of $SeO_2$ was dissolved in 40 mL DI water and stirred for 5 min. After this, we added a few drops of 37% HCl to maintain the pH in the range of 2–3. The electrodeposited sample was washed several times with DI water and then dried at 60 °C overnight. Furthermore, the dried sample was annealed at 200 °C in an argon environment for 2 h. Similarly, we fabricated a ruthenium cluster decorated nickel diselenide sample under similar experimental conditions. Additionally, the concentration of $RuCl_3 \cdot xH_2O$ in the solution was changed to 20 mmol, 30 mmol, 40 mmol, 50 mmol, and 60 mmol. Ru nanocluster decorated nickel diselenide samples are denoted as 20-Ru–$NiSe_2$, 30-Ru–$NiSe_2$, 40-Ru–$NiSe_2$, 50-Ru–$NiSe_2$, and 60-Ru–$NiSe_2$, respectively.

### Materials characterization

An X-Ray diffractometer (Empyrean, PANalytical) instrument with Cu Kα 1.54 Å is used to characterize the phase composition of all the prepared samples with a scan rate of 0.5 degree per min in the range of 20 to 80 degrees. A Nova scanning electron microscope (Nova Nano SEM 450) and transmission electron microscope (FEI Tecnai G2 F30 S-Twin TEM 300 kV) are used to analyze the surface morphology and elemental mapping of the samples. X-ray photoelectron spectroscopy (Omicron Nano Tech. XPS) with a Mg Kα source was performed to investigate the elemental composition and electronic state of all present elements. Finally, we performed inductively coupled plasma optical emission spectroscopy (PerkinElmer Optima 5300 DV ICP-OES) to analyze the ratio of ruthenium to nickel diselenide.

### Electrochemical characterization

The electrochemical performance of all the catalysts for the HER and OER was evaluated using a Biologic SAS VMP3 electrochemical workstation in nitrogen-saturated 1.0 M KOH solution, at room temperature, using a typical three-electrode setup. All prepared electrodes are used as working electrodes, a graphite rod, as the counter electrode, and a Hg/HgO electrode, as the reference electrode. The working electrode potential was converted to RHE using the Nernst equation ($E_{RHE} = E^0_{Hg/HgO} + 0.059 \times pH$).[9] All the polarization curves were recorded with 85% *IR* corrected by LSV at a scan rate of 2 mV $s^{-1}$. We carried out electrochemical impedance spectroscopy to calculate the charge transfer resistance of the materials in the frequency range of 50 mHz to 100 kHz. We obtained the electrochemically active surface area (ECSA) of all the prepared electrodes from the double-layer capacitance ($C_{dl}$), which was evaluated by scanning the CV in the non-faradaic potential region *vs.* Hg/HgO with different scan rates from 10 mV $s^{-1}$ to 100 mV $s^{-1}$. Pt/C and $IrO_2$ electrodes were studied as benchmark catalysts for the HER and OER, respectively, with 4 mg of Pt/C or $IrO_2$ in 1 mL solution (750 μL of DI water, 200 μL of IPA, and 50 μL of Nafion). The solution is

 

sonicated for 2 h to make a proper dispersion and then drop-coated over HCl-pretreated NF.

### Density functional theory calculations

All density functional theory calculations were performed using the Vienna *ab initio* simulation package (VASP)[48–51] within the framework of the generalized gradient approximation (Perdew–Burke–Ernzerhof (PBE) exchange–correlation functional).[52] To account for the core–valence electron interactions, we employed the projector augmented wave (PAW) method.[53] Furthermore, we incorporate the effects of van der Waals interactions *via* Grimme's D3 dispersion correction.[54] The kinetic energy cutoff for plane wave expansions, convergence criteria for energy, and forces on each atom were set to 550 eV, 10–5 eV and 0.01 eV $Å^{-1}$, respectively. To minimize possible interactions between the periodic images, a vacuum layer of 16 Å was added in the non-periodic direction. For a pure $NiSe_2$ system, a (210) surface slab with seven layers, consisting of 28 Ni and 56 Se atoms, was used. All layers were relaxed during geometry optimization. However, for the Ru nanocluster decorated $NiSe_2$ surface, a $Ru_8$ cluster was adsorbed on the $NiSe_2$ (210) surface slab with five layers, comprising 60 Ni, 120 Se, and 8 Ru atoms. For the pure $NiSe_2$ (210) and $Ru_8$–$NiSe_2$ (210) systems, the Brillouin zone integrations were carried out using $\Gamma$-centred $k$-point meshes of 4 × 9 × 1 and 5 × 5 × 1, respectively.

## Results and discussion

Synthesis of Ru nanocluster decorated nickel diselenide (Ru–$NiSe_2$) supported on nickel foam was performed through a single-step electrodeposition process, followed by low-temperature thermal annealing in an argon atmosphere, as illustrated in ESI Fig. S1.† The process involved a co-electrodeposition strategy using precursors of nickel and selenium along with varying concentrations of ruthenium(III) chloride of 20 mmol, 30 mmol, 40 mmol, 50 mmol, and 60 mmol, as detailed in the ESI Methods section.† We applied −1 V *vs.* Ag/AgCl for 10 min to obtain a mass loading of 2.42 mg $cm^{-2}$. Pristine $NiSe_2$ samples are grown under controlled conditions on Ni foam. All the electrodeposited samples are washed with DI water and annealed in an argon atmosphere at 200 °C for 2 h.

Fig. 1a shows the crystal structure of Ru nanocluster decorated nickel diselenide, which was confirmed from the X-ray diffraction (XRD) analysis (Fig. 1b). Three high-intensity peaks at 44.44, 51.78, and 76.27 correspond to the reflections from nickel foam (PDF no.-98-012-3812) (Fig. S2†).[55] The other marked peaks correspond to the cubic phase of $NiSe_2$ (PDF no.-00-041-1495),[56] which seems to have remained unchanged with Ru decoration, indicative of no structural changes in $NiSe_2$. We performed inductively coupled plasma optical emission spectroscopy (ICP-OES) to analyze the ruthenium content in nickel

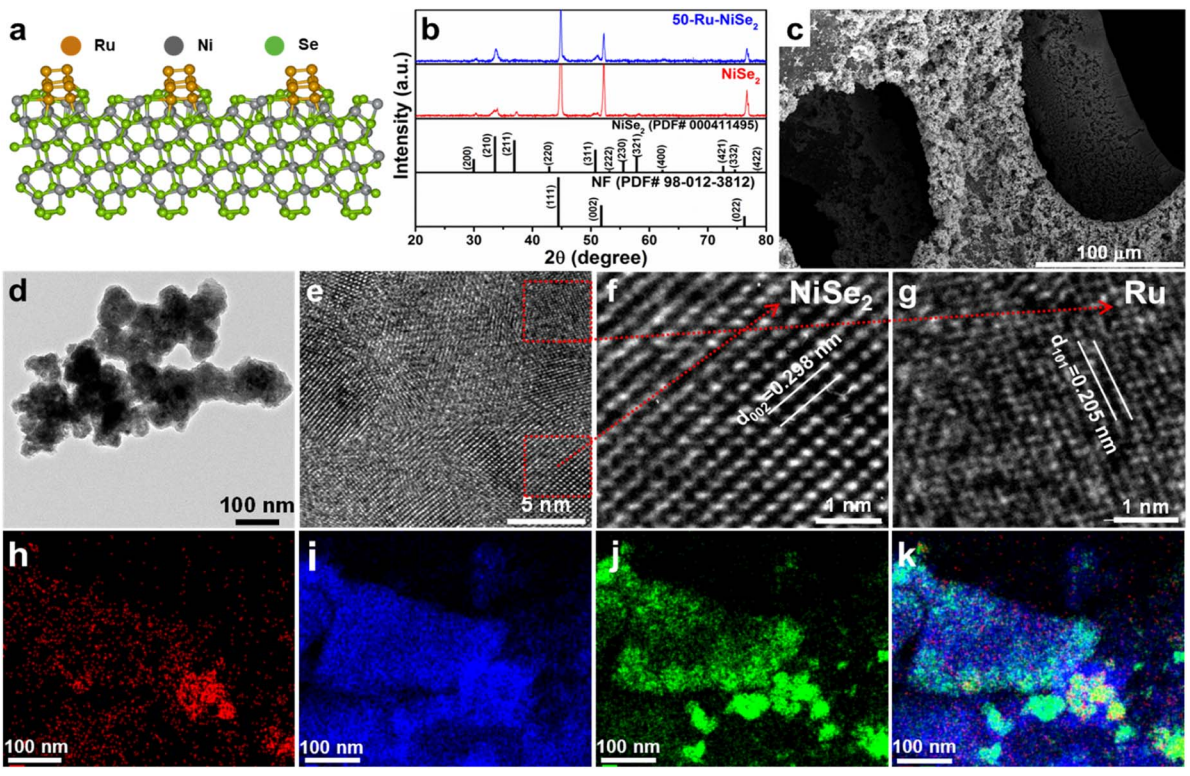


Fig. 1 Phase and morphology analyses of Ru nanocluster decorated nickel diselenide. (a) Crystal structure of ruthenium nanocluster decorated nickel diselenide. (b) XRD pattern of $NiSe_2$ and 50-Ru–$NiSe_2$. (c) SEM images of 50-Ru–$NiSe_2$. (d) TEM image of 50-Ru–$NiSe_2$. (e) HRTEM image of 50-Ru–$NiSe_2$. (f and g) HRTEM images showing the interplanar spacing for $NiSe_2$ and Ru nanoclusters, respectively. (h–j) Elemental mapping of Ru, Ni, and Se, respectively. (k) Elemental mapping of Ru, Ni, and Se, together.

diselenide. For the 50-Ru–$NiSe_2$ sample (with an initial concentration of 50 mmol ruthenium(III) chloride), a Ru content of 3.9 wt% was confirmed.

The morphology of all the prepared catalysts was further analyzed by scanning electron microscopy (SEM) and transmission electron microscopy (TEM). For instance, Fig. 1c shows the SEM image of the surface of nickel foam which is fully covered with electrodeposited 50-Ru–$NiSe_2$. Fig. 1d shows the TEM image of 50-Ru–$NiSe_2$. The corresponding high-resolution TEM (HR-TEM) images given in Fig. 1e–g clearly reveal interplanar spacing of $NiSe_2$ and Ru nanoclusters with the corresponding lattice planes.[46,57] SEM images of electrodeposited $NiSe_2$ over NF (Fig. S3†) with uniform growth of $NiSe_2$ over the NF surface and the corresponding energy-dispersive spectroscopy (EDX) mapping showed uniform distribution of nickel and selenium over the surface (Fig. S4†). The TEM image shown in Fig. S5† displays the morphology of $NiSe_2$ along with the corresponding *d* spacing. Besides the morphological studies, energy-dispersive spectroscopy (EDX) analysis is also performed in order to confirm the elemental composition in the sample. The uniform distribution of Ru, Ni, and Se over the surface was confirmed from the elemental mapping images shown in Fig. 1h–k, respectively. X-ray photoelectron spectroscopy (XPS) is a powerful technique to analyze the chemical composition and chemical state of the elements present in the sample. XPS measurements were carried out for $NiSe_2$, and 50-Ru–$NiSe_2$. Due to the spin–orbit coupling, Ni, Ru, and Se peaks split into Ni $2p_{1/2}$, Ni $2p_{3/2}$, Ru $3p_{1/2}$, Ru $3p_{3/2}$; Se $3d_{5/2}$, and Se $3d_{3/2}$, respectively.[46,47,56] In Fig. 2a, the XPS survey spectrum of $NiSe_2$ shows the presence of Ni and Se, while that of 50-Ru–$NiSe_2$ shows the presence of Ru, Ni, and Se. Fig. 2b and c show the high-resolution XPS spectra of $NiSe_2$, and Fig. 2d–f show the high-resolution XPS spectra of 50-Ru–$NiSe_2$. The peaks at 854.5 eV and 872.3 eV are assigned to $Ni^{2+}$ $2p_{3/2}$ and $Ni^{2+}$ $2p_{1/2}$, respectively, while the two broad peaks at 859.4 eV and 877.8 eV correspond to the satellite peak of Ni 2p (Fig. 2b).[58] Fig. 2c shows the XPS peaks at 55.3 eV and 56.4 eV which correspond to Se $3d_{5/2}$ and Se $3d_{3/2}$, and a broad peak observed at 59.4 eV reveals partial oxidation of selenium.[59,60] Fig. 2d shows the high-resolution XPS peaks at 461.8 eV and 484.2 eV, corresponding to $Ru^0$ $3p_{3/2}$ and $Ru^0$ $3p_{1/2}$ from metallic Ru,[61] which further indicates the formation of ruthenium nanoclusters. High-resolution XPS peaks observed at 854.8 eV and 872.6 eV in Fig. 2e are assigned to $Ni^{2+}$ $2p_{3/2}$ and $Ni^{2+}$ $2p_{1/2}$, respectively, and the two broad peaks at 860.2 eV and 878.6 eV correspond to the satellite peak of Ni 2p.[58,62] Fig. 2f shows XPS peaks at 55.3 eV and 56.4 eV which correspond to Se $3d_{5/2}$, and Se $3d_{3/2}$, respectively, and a broad peak seen at 59.3 eV reveals partial oxidation of selenium.[59,60,63] A positive shift of +0.3 eV is observed in the high-resolution nickel spectra of 50-Ru–$NiSe_2$ upon Ru incorporation. This indicates that there is charge transfer happening from nickel to ruthenium in 50-Ru–$NiSe_2$, which is originated from the high electronegativity of Ru (2.5) compared to that of Ni (1.2).[46,64] This further indicates the presence of an electrostatic interaction between Ni and Ru in the Ru nanocluster incorporated sample.

The electrochemical performance of the catalysts was studied in nitrogen-saturated 1.0 M KOH electrolyte using linear sweep voltammetry (LSV) at 2 mV $s^{-1}$. Improvement in the electrocatalytic performance of the Ru-incorporated $NiSe_2$ catalysts in comparison with their pristine counterpart towards the HER was clearly confirmed through detailed LSV studies

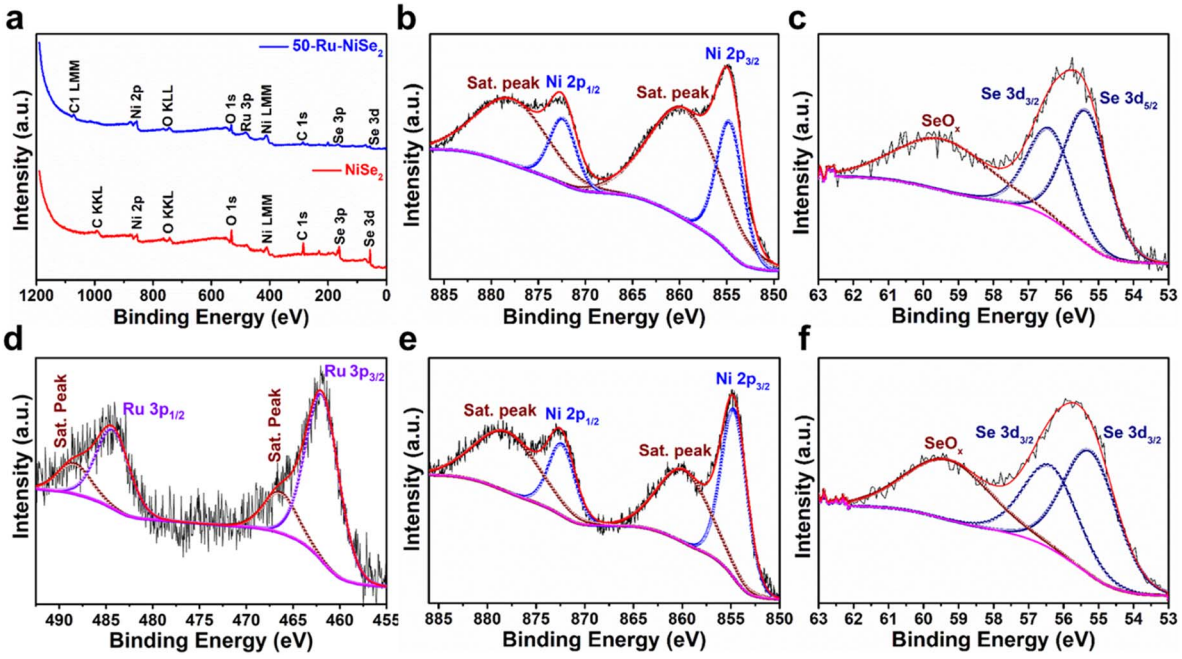


Fig. 2 XPS analysis. (a) Survey spectra of $NiSe_2$ and 50-Ru–$NiSe_2$. (b and c) High-resolution XPS spectra of Ni and Se of $NiSe_2$. (d–f) High-resolution XPS spectra of Ru, Ni, and Se of 50-Ru–$NiSe_2$.

 

performed on the catalysts with varying molar ruthenium contents (Ru = 10 mmol, 20 mmol, 30 mmol, 40 mmol, 50 mmol, and 60 mmol), as shown in Fig. S6.† The catalyst with an initial molar Ru content of 50 mmol (50-Ru–$NiSe_2$) showed the best performance among all the studied catalysts. Based on this, detailed electrocatalytic performance evaluation on bare NF, $NiSe_2$ sheets and 50-Ru–$NiSe_2$ was carried out along with 20 wt% Pt/C (Pt/C) as the reference. As shown in Fig. 3a, *IR*-compensated linear sweep voltammetry was performed to analyze the alkaline HER activity of all the prepared catalysts. 50-Ru–$NiSe_2$ showed excellent activity with a very low overpotential of 13 mV and 103 mV at current densities of 10 mA $cm^{-2}$ and 100 mA $cm^{-2}$, respectively. The obtained values are much better in comparison to those of the benchmark Pt/C catalyst, which showed overpotentials of 28 mV and 151 mV, at the respective current densities of 10 mA $cm^{-2}$ and 100 mA $cm^{-2}$. While $NiSe_2$ showed an overpotential of 180 mV and 338 mV, NF exhibited poor activity with overpotentials of 293 mV and 483 mV at the respective current densities of 10 mA $cm^{-2}$ and 100 mA $cm^{-2}$. To understand the electrochemical kinetics for the HER, we investigated the Tafel slopes for all the catalysts. In general, there are three steps involved in the HER process;[65]

$$M^* + H_2O + e^- \rightarrow M\text{–}H + OH^- \text{ (Volmer step)} \quad (1)$$

$$H_2O + M\text{–}H + e^- \rightarrow M^* + H_2 + OH^- \text{ (Heyrovsky step)} \quad (2)$$

$$M\text{–}H + M\text{–}H \rightarrow H_2 + 2M^* \text{ (Tafel step)} \quad (3)$$

The Tafel slopes obtained from the corresponding LSV plots of all the studied samples are depicted in Fig. 3b, which further confirmed the superior HER activity of 50-Ru–$NiSe_2$ (21 mV $dec^{-1}$), compared to Pt/C (29 mV $dec^{-1}$), $NiSe_2$ (128 mV $dec^{-1}$), and, NF (137 mV $dec^{-1}$). The low Tafel slopes of 50-Ru–$NiSe_2$ and Pt/C reveal that the HER process for these two systems follows the Volmer–Tafel mechanism. As further indicated in Fig. 3c, from the comparison of overpotentials for the HER at different current densities of 10 mA $cm^{-2}$, 50 mA $cm^{-2}$, and 100 mA $cm^{-2}$ for all the studied catalysts, 50-Ru–$NiSe_2$ exhibits the lowest overpotential, which is better than all the best-reported values for alkaline HER (Table S1, ESI†). Electrochemical impedance spectroscopy was performed to understand the reaction kinetics for charge transfer between the interface of the catalyst surface and the electrolyte. 50-Ru–$NiSe_2$ showed a lower charge transfer resistance ($R_{ct}$) of 4.03 ohms, as compared to $NiSe_2$, at an overpotential of −100 mV (Fig. 3d). Chronoamperometry was performed to understand the electrochemical stability of the catalyst. 50-Ru–$NiSe_2$ showed excellent stability with negligible change in current density after a 20 h stability test at a current density of 65 mA $cm^{-2}$ (Fig. 3e). This clearly indicates the catalyst's exceptional durability in alkaline media for high current density performance. In Fig. 3f, we showed a comparison of LSV plots recorded for 50-Ru–$NiSe_2$ at the initial cycle and after the 20 h chronoamperometry test. The overlapping curves further indicate the high durability of the catalyst under long-term operating conditions, which is an essential parameter for the overall water-splitting process. High electrocatalytic activity and stability of 50-Ru–$NiSe_2$ in alkaline media make this catalyst an efficient candidate for the HER.

We further explored the OER activity of all the catalysts in 1.0 M KOH electrolyte. The *IR*-compensated LSVs are plotted in Fig. 4a to analyze the OER activity of all the studied catalysts. 50-Ru–$NiSe_2$ showed the best OER performance with a low

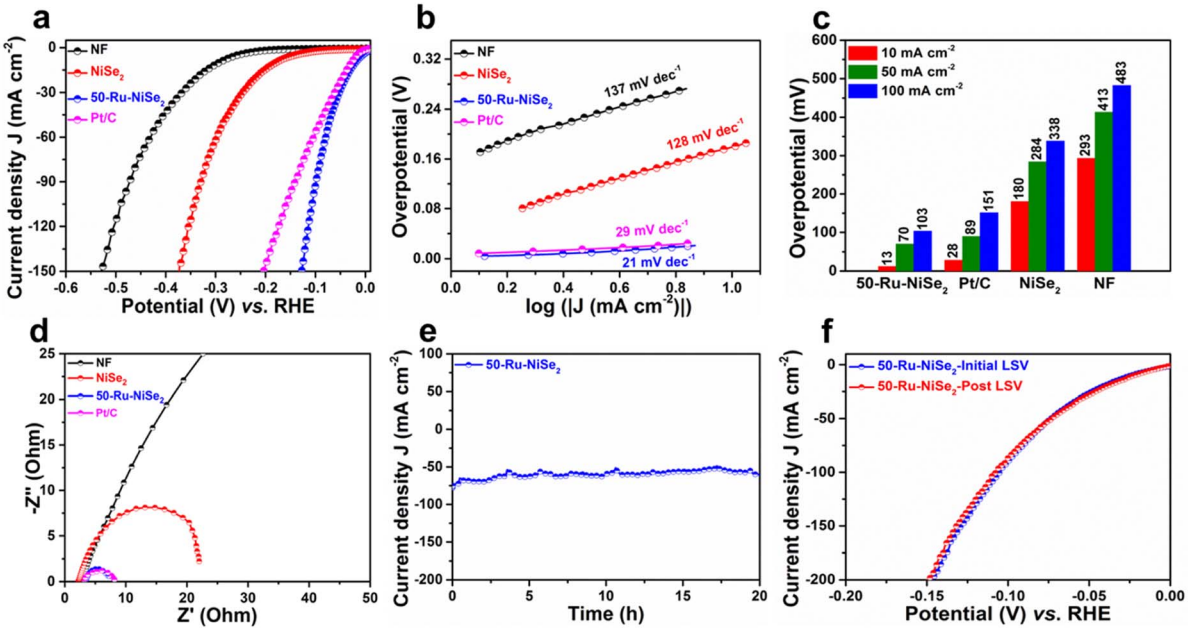


Fig. 3 HER studies. (a) LSV polarization curves recorded for NF, $NiSe_2$, 50-Ru–$NiSe_2$, and Pt/C. (b) The corresponding Tafel plots. (c) Overpotential measured at current densities of 10, 50, and 100 mA $cm^{-2}$. (d) Comparison of Nyquist plots of NF, $NiSe_2$, 50-Ru–$NiSe_2$ and Pt/C. (e) Stability plot of 50-Ru–$NiSe_2$ obtained using chronoamperometry measurements. (f) Initial and post LSV plots of 50-Ru–$NiSe_2$.

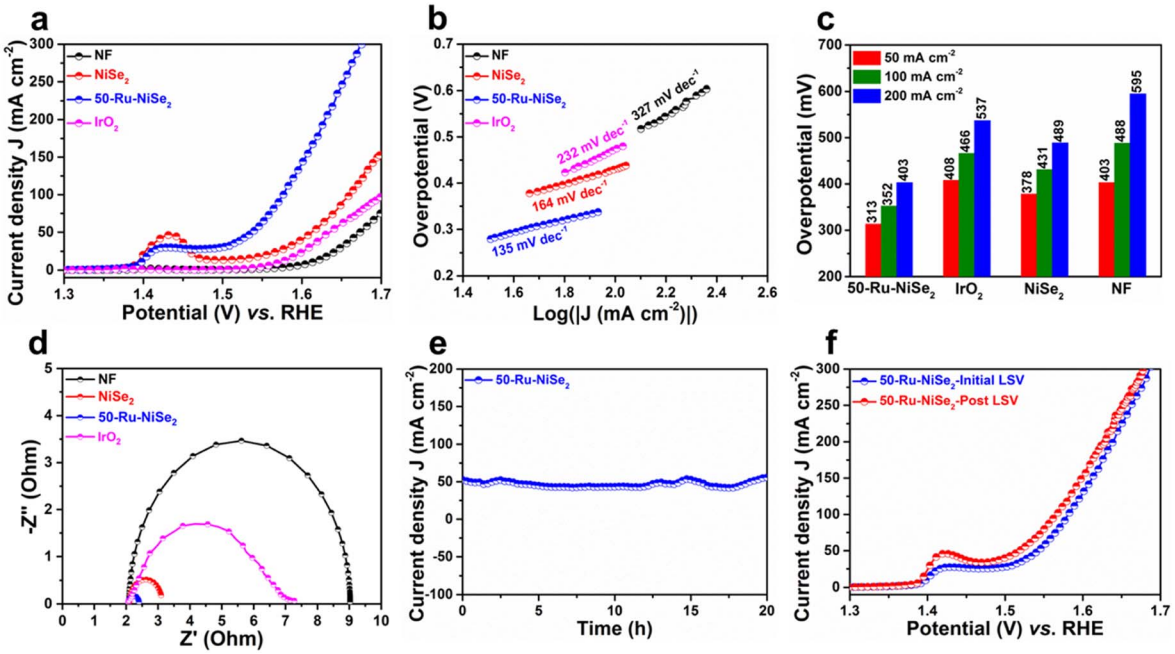


Fig. 4 OER studies. (a) LSV polarization curves of NF, $NiSe_2$, 50-Ru–$NiSe_2$, and $IrO_2$ and (b) the corresponding Tafel plots. (c) Corresponding overpotential recorded at current densities of 10, 50, and 100 mA $cm^{-2}$. (d) Nyquist plots of NF, $NiSe_2$, $IrO_2$ and 50-Ru–$NiSe_2$. (e) Stability plots of 50-Ru–$NiSe_2$ obtained using chronoamperometry measurements. (f) Initial and post LSV plots of 50-Ru–$NiSe_2$.

overpotential of 313 mV and 352 mV at current densities of 50 mA $cm^{-2}$ and 100 mA $cm^{-2}$, respectively, as compared to $NiSe_2$ (378 mV and 431 mV) and NF (403 mV and 488 mV). The OER performance of the studied catalyst was better than that of the benchmark catalyst $IrO_2$. The electrochemical kinetics of these materials for the OER mechanism was investigated by using Tafel slopes.

Fig. 4b shows the Tafel slopes of all the studied catalysts. 50-Ru–$NiSe_2$ exhibited a low Tafel slope (135 mV $dec^{-1}$), compared to $IrO_2$ (232 mV $dec^{-1}$), $NiSe_2$ (164 mV $dec^{-1}$), and, NF (327 mV $dec^{-1}$), indicative of its high OER kinetics. The overpotentials for the OER of all the catalysts recorded at different current densities of 50 mA $cm^{-2}$, 100 mA $cm^{-2}$, and 200 mA $cm^{-2}$ are plotted in Fig. 4c, which showed that 50-Ru–$NiSe_2$ exhibits the lowest overpotential compared to the other three electrodes ($IrO_2$, $NiSe_2$, and NF), which is also better than the recently reported values for alkaline OER from the literature (Table S2, ESI†). Electrochemical impedance spectroscopy was performed (Fig. 4d) to understand the reaction kinetics for charge transfer between the interface of the catalyst surface and the electrolyte. 50-Ru–$NiSe_2$ showed a lower charge transfer resistance ($R_{ct}$) of 0.34 ohm as compared to $NiSe_2$ and $IrO_2$ at an overpotential of 300 mV.

The chronoamperometry test was performed (Fig. 4e) to evaluate the stability of the catalyst. 50-Ru–$NiSe_2$ showed a very small change in current density after a 20 h stability test at a current density of 50 mA $cm^{-2}$, confirming its very good durability in alkaline media for high current density performance. In Fig. 4f, we compared the LSVs recorded for 50-Ru–$NiSe_2$ after a 20 h chronoamperometry test along with that of the initial cycle, which did not show much significant change, clearly revealing the high durability of the catalyst under long-term operating conditions. High electrocatalytic activity and stability of 50-Ru–$NiSe_2$ in alkaline media make this catalyst an efficient and stable candidate for the OER. After the stability test, we further performed XPS and SEM characterization studies to understand the surface reconstruction process. The post-cycling high-resolution XPS spectra show several changes in peak intensity and peak positions. The Ru 3p peaks show a slight positive shift as compared to those of metallic ruthenium (Fig. S7†), which indicates the oxidation of ruthenium.[61] Similarly, the Ni 2p peak also exhibits a positive shift, indicating the formation of $Ni^{3+}$ species from $Ni^{2+}$ as shown in Fig. S8.†[66] This positive shift confirms the conversion of the surface of nickel diselenide to nickel oxyhydroxide. Furthermore, there is a stronger oxidation peak observed in the Se 3d spectrum (Fig. S9†) compared to the initial state. This suggests that the selenium surface has undergone reconstruction to form $SeO_x$ species.[67] To gain a better understanding of the surface reconstruction, the upper surface of the catalysts was etched with argon, and XPS analysis data were recorded from the inner layer of the catalysts. After 10 minutes of etching, the metallic ruthenium peak becomes clearly visible, indicating the presence of metallic ruthenium. The $Ni^{2+}$ oxidation peaks corresponding to Ni $2p_{3/2}$ and Ni $2p_{1/2}$ are also observed. However, the oxidation peak for selenium disappears, indicating the absence of selenium oxide formation. Based on this XPS analysis, it can be concluded that the surface of $NiSe_2$ has been converted from $NiSe_2$ to $Ni(OOH)_x$, while the inner core of the catalyst still remains in the $NiSe_2$ phase. The $Ni(OOH)_x$ species serve as the active sites during the OER process, while the highly conductive inner core of $NiSe_2$ facilitates charge migration.

 

Additionally, we performed the SEM analysis after the OER stability tests (Fig. S10†). Fig. S10a–d† show the SEM images of 50-Ru–$NiSe_2$ before and after the OER stability test. Few changes occurred after the OER stability test during the surface reconstruction process. Inspired by the enhanced bifunctional electrochemical HER and OER activities of 50-Ru–$NiSe_2$ in alkaline media, we designed an electrolyzer for overall alkaline water splitting with 50-Ru–$NiSe_2$ as both the anode and cathode (50-Ru–$NiSe_2$//50-Ru–$NiSe_2$). The polarization curves recorded for the 50-Ru–$NiSe_2$//50-Ru–$NiSe_2$ and $NiSe_2$//$NiSe_2$ system are compared with that of Pt/C//$IrO_2$, the benchmark catalyst (Fig. 5a). 50-Ru–$NiSe_2$//50-Ru–$NiSe_2$ showed a remarkably low cell potential of 1.45 V to achieve a current density of 10 mA $cm^{-2}$, while Pt/C//$IrO_2$ delivers the same current density at a higher potential of 1.58 V. $NiSe_2$//$NiSe_2$ required a much higher potential of 1.66 V to achieve 10 mA $cm^{-2}$ current density. The full cell potentials required to obtain current densities of 10 mA $cm^{-2}$, 50 mA $cm^{-2}$, and 100 mA $cm^{-2}$ for 50-Ru–$NiSe_2$//50-Ru–$NiSe_2$, $NiSe_2$//$NiSe_2$, and benchmark Pt/C//$IrO_2$ are depicted in Fig. 5b. We performed the durability test for the full cell in Fig. 5c, and 50-Ru–$NiSe_2$//50-Ru–$NiSe_2$ showed impressive long-term durability with high current retention even after 400 h at an applied potential of 1.45 V, clearly revealing excellent performance for overall water splitting. We compared the performance of our system with that of most recently reported alkaline bifunctional electrocatalysts (at 10 mA $cm^{-2}$), and the present data were found to be superior (Fig. 5d). The details are provided in Table S3 (ESI).† The long-term stability test was extended for a month with continuous operation, and 50-Ru–$NiSe_2$//50-Ru–$NiSe_2$ exhibited exceptional stability for alkaline water splitting (Fig. S7†). To understand the intrinsic activity of the catalyst, we calculated the electrochemically active surface area (ECSA) of the synthesized catalysts from the charge double layer capacitance $C_{dl}$ (ESI, Note S2†). CV is carried out in the non-faradaic region of the potential with different scan rates in the alkaline electrolyte (Fig. S8†). The CVs recorded at 10 mV $s^{-1}$ for 50-Ru–$NiSe_2$ showed a much higher current density than those of $NiSe_2$, suggesting higher $C_{dl}$ of 50-Ru–$NiSe_2$ compared to $NiSe_2$. The $C_{dl}$ of NF, $NiSe_2$, and 50-Ru–$NiSe_2$ is measured to be 1.2 mF $cm^{-2}$, 11.6 mF $cm^{-2}$, and, 71.3 mF $cm^{-2}$, respectively (Table S4, ESI†).

## Theoretical studies

To obtain further insights on the remarkably enhanced bifunctional catalytic activity of Ru nanocluster-decorated $NiSe_2$ over pristine $NiSe_2$ towards the HER and OER in an alkaline

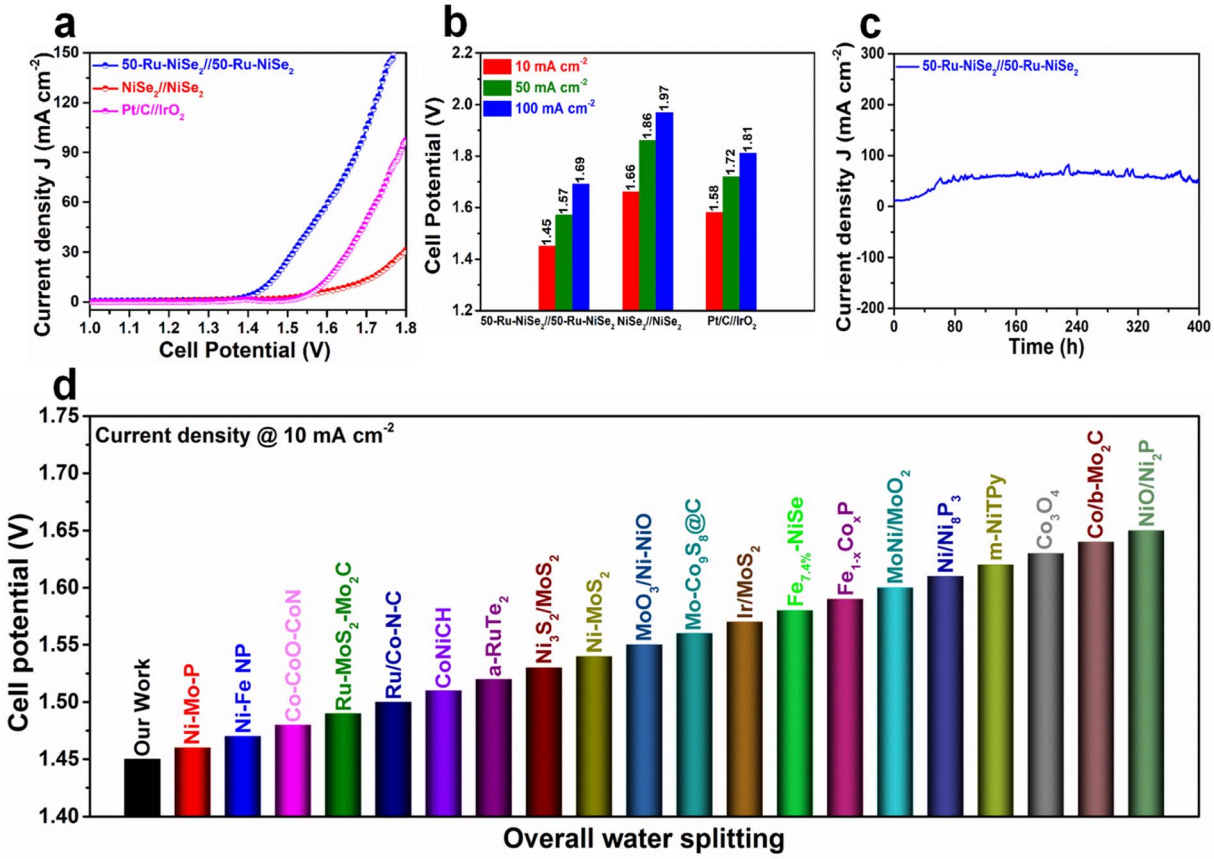


Fig. 5 Overall water splitting studies. (a) Comparison of LSV plots of 50-Ru–$NiSe_2$//50-Ru–$NiSe_2$, and $NiSe_2$//$NiSe_2$ with those of benchmark Pt/C//$IrO_2$. (b) Cell potentials required to obtain current densities of 10 mA $cm^{-2}$, 50 mA $cm^{-2}$, and 100 mA $cm^{-2}$ for 50-Ru–$NiSe_2$//50-Ru–$NiSe_2$, $NiSe_2$//$NiSe_2$ and Pt/C//$IrO_2$. (c) Stability plots of 50-Ru–$NiSe_2$//50-Ru–$NiSe_2$ were obtained using a chronoamperometry test. (d) Comparison of the full-cell performance of our work with those of the best reported alkaline catalysts (Table S4, ESI†).

medium, we employed first-principles DFT calculations. Since the as-prepared samples are large and computationally challenging to handle with DFT, we chose to study systems of reasonable sizes that can be feasibly analyzed. We believe that our model systems are sufficient to capture the fundamental chemical processes that underlie the observed catalytic behavior. Specifically, we investigated the HER and OER catalytic activities of the clean $NiSe_2$ (210) surface and $NiSe_2$ (210) surface decorated with a Ru nanocluster. The reason for choosing the (210) plane of $NiSe_2$ is that the experimentally observed XRD pattern for $NiSe_2$ indicates that the peak with the maximum intensity corresponds to the (210) plane (see Fig. 1b). Furthermore, it is clear from this figure that the XRD pattern remains unchanged with Ru nanocluster decoration. Therefore, for both pristine $NiSe_2$ and Ru nanocluster-decorated $NiSe_2$, we opted to study the (210) plane. Moreover, to examine the effect of Ru nanocluster decoration on the catalytic activity of $NiSe_2$ (210) towards the HER and OER, we chose an 8-atom Ru nanocluster. In the absence of a clear indication from the experiments about how the Ru dopants are arranged on the surface, we consider a $Ru_8$ nanocluster adsorbed $NiSe_2$ (210) surface as a model catalyst. The choice of this particular size for the nanocluster is guided by the findings in published literature,[68–70] which suggest that $Ru_8$ is relatively more stable when compared to neighboring nanocluster sizes, and also takes into consideration the computational tractability. To compare the catalytic activities of clean and $Ru_8$ adsorbed $NiSe_2$ (210) surfaces, we consider the structures shown in Fig. S9.† We adsorbed all the relevant intermediate atoms/molecules involved in these reactions on all the available high-symmetry sites of these two systems. In the case of pure $NiSe_2$, these sites include Se-top, Ni-top, and Se–Se bridge positions. However, in $Ru_8$–$NiSe_2$, there exists additional sites referred to as Ru-top and Ru–Ru bridge. All of these sites are marked in Fig. S9.† The complete HER in an alkaline medium is $4H_2O + 4e^- \rightarrow 2H_2 + 4OH^-$. As shown by Nørskov *et al.*, the free energy of H adsorption, $\Delta G_{H^*}$, is a good descriptor for characterizing the catalytic activity of transition metal-based materials towards the HER in acidic electrolytes.[71,72] According to their results, adsorption-free energy of H, $\Delta G_{H^*}$ close to zero is a necessary criterion for a catalyst to be considered suitable for acidic HER. We adopt the criterion of $|\Delta G_{H^*}| \leq 0.2$ eV to identify the potential candidates for the HER in an acidic medium. However, in an alkaline medium, $\Delta G_{H^*}$ alone is insufficient to fully characterize the HER activity. This is because of the low availability of $H^+$ ions in an alkaline medium, where the dissociation of $H_2O$ into $H^+$ and $OH^-$ becomes an essential part of the HER and contributes additional energy to the overall reaction Gibbs free energy. Furthermore, there is currently no single descriptor in the literature that adequately describes the HER activity of a material in an alkaline medium. Therefore, in addition to the $|\Delta G_{H^*}| \leq 0.2$ eV criterion, we consider the following factors to assess the HER activity in alkaline environments:

(i) The binding energy of $H_2O$ with the material surface, (ii) the feasibility of $H_2O$ dissociation into $H^+$ and $OH^-$, and (iii) the free energy of OH adsorption, $\Delta G_{OH^*}$, which should ideally be close to zero according to the Sabatier principle.[73] First, we calculate the value of $\Delta G_{H^*}$ using the following equation:

$$\Delta G_{H^*} = E_{ads}(H) + 0.24 \text{ eV}, \quad (4)$$

where $E_{ads}(H)$ represents the adsorption energy of the H atom on either the pure or $Ru_8$ cluster decorated $NiSe_2$. Please check the ESI (Note S3)† for more details. The visual representation of $\Delta G_{H^*}$ at different sites on both pristine $NiSe_2$ and $Ru_8$–$NiSe_2$ is given in Fig. 6a. We observe from this figure that in both the pristine and $Ru_8$–$NiSe_2$ materials, the value of $\Delta G_{H^*}$ lies close to zero. The value of $\Delta G_{H^*}$ closest to zero is 0.08 eV for the pristine material, while it is 0.04 eV for $Ru_8$–$NiSe_2$. We also note that, in the case of the pristine material, the $|\Delta G_{H^*}| \leq 0.2$ eV criterion is satisfied only at the Se-top sites. On the other hand, for $Ru_8$–$NiSe_2$, in addition to a few Se-top positions, almost all sites, including Ru-top and Ru–Ru bridge positions of the Ru cluster, are HER active in terms of $\Delta G_{H^*}$. Therefore, based on the H adsorption free energy plot, we can conclude that both pristine and $Ru_8$–$NiSe_2$ (210) are HER active; however, the number of active sites is more in the case of the Ru cluster-decorated surface. Next, we examine the binding of $H_2O$ molecules with the pristine and $Ru_8$-decorated $NiSe_2$ (210) surfaces. To characterize this interaction, we calculate the adsorption energy, $E_{ads}(H_2O)$, of an $H_2O$ molecule using the following equation.

$$E_{ads}(H_2O) = E(H_2O^*) - E(^*) - E(H_2O) \quad (5)$$

In this equation, $E(H_2O^*)$ represents the total energy of the adsorbed $H_2O$ molecule on either $NiSe_2$ or $Ru_8$–$NiSe_2$. $E(^*)$ is the total energy of these systems prior to $H_2O$ adsorption, and $E(H_2O)$ represents the total energy of a free $H_2O$ molecule. A negative value of $E_{ads}(H_2O)$ would indicate that the adsorption of $H_2O$ on the catalyst surface is exothermic. Values of $E_{ads}(H_2O)$ at some of the possible sites of $NiSe_2$ and $Ru_8$–$NiSe_2$ (210) are given in Table S5 (ESI).† From this table, it is clear that the maximum $H_2O$ adsorption energy is $-0.83$ eV on one of the Ni-top sites of pristine $NiSe_2$. However, in the case of $Ru_8$–$NiSe_2$, the strongest binding ($E_{ads}(H_2O) = -1.08$ eV) occurs on one of the Ru-top positions. This shows that an $H_2O$ molecule is significantly more strongly adsorbed on $Ru_8$–$NiSe_2$ (210) compared to on the pristine material. While the optimal value is not known, it is conceivable that the strong binding energy of $H_2O$ could facilitate its dissociation at the surface, subsequently aiding the Heyrovsky or Tafel steps in the HER process. Next, we proceed to assess whether the dissociation of an $H_2O$ molecule is energetically favorable on $NiSe_2$ (210) and $Ru_8$–$NiSe_2$ (210). The reaction energy, $\Delta E$, determines whether a reaction is energetically favorable. We calculate the value of $\Delta E$ according to $E(H^* + OH^*) - E(H_2O^*)$. The lowest possible pathways for $H_2O$ dissociation on the pristine and $Ru_8$ cluster decorated $NiSe_2$ surfaces are presented in Fig. 7. From this figure, it is evident that the value of $\Delta E$ on $NiSe_2$ (210) is 0.76 eV. This significant positive value of $\Delta E$ indicates that the $H_2O$ dissociation into H and OH is an endothermic process. On the other hand, on the $Ru_8$–$NiSe_2$ system, the dissociation of a $H_2O$

 

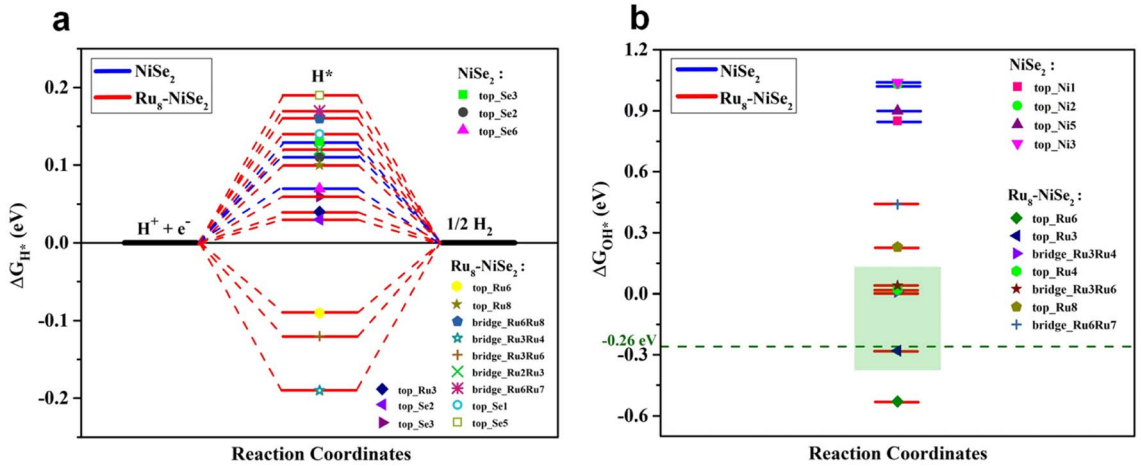


Fig. 6 Theoretical calculations for the HER. (a) Free energy plots for H adsorption and (b) OH adsorption on some of the high symmetry sites of pristine and $Ru_8$–$NiSe_2$ (210) surfaces.

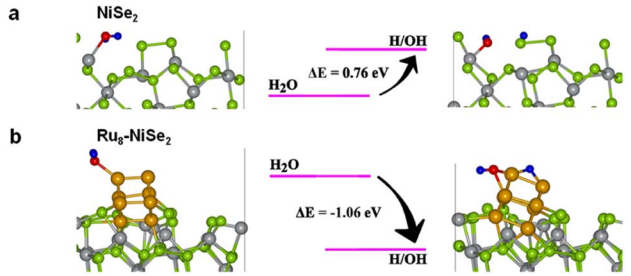


Fig. 7 Representation of reaction pathways. (a) Pristine and (b) $Ru_8$–$NiSe_2$ (210) materials. Green, grey, golden yellow, red, and blue coloured balls represent Se, Ni, Ru, O, and H atoms, respectively.

molecule into H and OH fragments yields a reaction energy of −1.06 eV, which is significantly negative. This indicates that $H_2O$ dissociation is exothermic and thus energetically feasible on the cluster-decorated $NiSe_2$ surface. As we have established that $H_2O$ is adsorbed more strongly on the $Ru_8$–$NiSe_2$ system and its dissociation into H and OH is energetically favorable on this system, we expect that the OH fragment will also be adsorbed more strongly on the Ru cluster-decorated surface compared to on pristine $NiSe_2$, where $H_2O$ adsorption is weaker and $H_2O \rightarrow H + OH$ is endothermic. To verify this assumption, we will now proceed to calculate the adsorption-free energy of OH, $\Delta G_{OH^*}$, on both the pristine and $Ru_8$–$NiSe_2$ materials. To calculate $\Delta G_{OH^*}$, we use the following equation:

$$\Delta G_{OH^*} = E_{ads}(OH) + 0.35\ \text{eV}. \quad (6)$$

Here, $E_{ads}(OH)$ denotes the adsorption energy of OH on either pure or $Ru_8$–$NiSe_2$ (210). More details are given in the ESI.† The values of $\Delta G_{OH^*}$ at various possible positions on both the systems are provided in Table S6 (ESI)† and the corresponding plot is presented in Fig. 6b. From this figure, it is clear that the value of $\Delta G_{OH^*}$ is highly positive, nearly 1.0 eV, close to zero and even slightly negative at some of the positions on the $Ru_8$–$NiSe_2$ surface. For example, at the $Ru_3$-top site, $\Delta G_{OH^*} = -0.28$ eV. Koper *et al.*[73] showed that transition metal decorated stepped surfaces of Pt have the best HER performance in alkaline media when $\Delta G_{OH^*} = -0.26$ eV. While there is no knowledge of what would be an optimal $\Delta G_{OH^*}$ on pristine or decorated $NiSe_2$ surfaces, one can take −0.26 eV as a guide. Since $\Delta G_{OH^*}$ on the Ru cluster-decorated surface is very close to the optimum value (see Fig. 6b), we expect $Ru_8$–$NiSe_2$ (210) to perform much better for the HER in alkaline media compared to pristine $NiSe_2$ (210). From the above discussion, we find that in terms of H adsorption, $\Delta G_{H^*}$ is approximately zero for both pristine and Ru cluster-decorated $NiSe_2$; however $Ru_8$–$NiSe_2$ (210) has more active sites compared to the pristine material. Moreover, the adsorption of an $H_2O$ molecule is comparatively stronger on $Ru_8$–$NiSe_2$ (210) than on pristine $NiSe_2$ (210). The most crucial step of $H_2O$ dissociation into H and OH is an exothermic process on $Ru_8$–$NiSe_2$, whereas it is endothermic on the pristine catalyst surface. Additionally, $\Delta G_{OH^*}$ is closer to the optimum value of −0.26 eV on $Ru_8$–$NiSe_2$ (210) while it is large and positive on the pristine material. These findings collectively suggest that Ru cluster-decorated $NiSe_2$ (210) is a significantly superior catalyst for alkaline HER compared to pristine $NiSe_2$ (210).

The OER in an alkaline medium involves the transfer of four electrons, accompanied by the formation of the O–O bond and the breaking of the O–H bond. The complete oxygen evolution reaction in an alkaline medium can be represented as $4OH^- \leftrightarrow 2H_2O + O_2 + 4e^-$ and the intermediate reaction steps are as follows:

$$* + OH^- \rightarrow OH^* + e^- \quad (7)$$

$$OH^* + OH^- \rightarrow O^* + H_2O + e^- \quad (8)$$

$$O^* + OH^- \rightarrow OOH^* + e^- \quad (9)$$

$$OOH^* + OH^- \rightarrow O_2 + * + H_2O + e^- \quad (10)$$

In summary, the OER follows the following path: $OH^- \rightarrow OH^* \rightarrow O^* \rightarrow OOH^* \rightarrow O_2$. The free energy change at each of

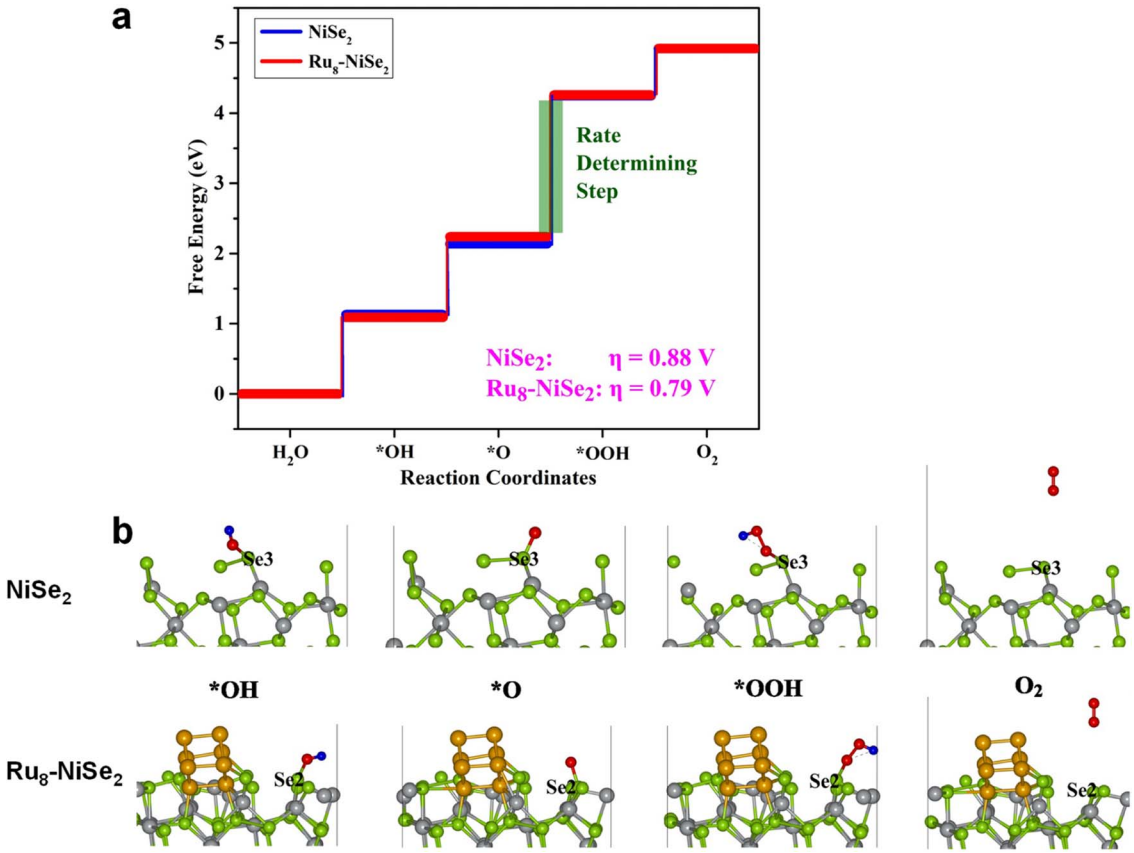


Fig. 8 Theoretical calculations for the OER. (a) Free energy plot and (b) intermediate structures involved in the OER at the minimum overpotential sites of pure and $Ru_8$–$NiSe_2$ (210) systems.

these reaction steps is calculated using the following equations. A more detailed discussion of these steps is provided in the ESI.†

$$\Delta G_1 = G(\mathrm{OH}^*) - G(^*) - G(\mathrm{OH}^- - \mathrm{e}^-) \quad (11)$$

$$\Delta G_2 = G(\mathrm{O}^*) + G(\mathrm{H_2O}) - G(\mathrm{OH}^*) - G(\mathrm{OH}^- - \mathrm{e}^-) \quad (12)$$

$$\Delta G_3 = G(\mathrm{OOH}^*) - G(\mathrm{O}^*) - G(\mathrm{OH}^- - \mathrm{e}^-) \quad (13)$$

$$\Delta G_4 = G(^*) + G(\mathrm{O_2}) + G(\mathrm{H_2O}) - G(\mathrm{OOH}^*) - G(\mathrm{OH}^- - \mathrm{e}^-) \quad (14)$$

Once we have the values of $\Delta G_1$, $\Delta G_2$, $\Delta G_3$, and $\Delta G_4$, we can calculate the overpotential, $\eta$, using the following equation: $\eta = \max[\Delta G_1, \Delta G_2, \Delta G_3, \Delta G_4]/e - 1.23$ V. We studied the adsorption of all the intermediates, that is, OH, O, and OOH, at all the possible non-equivalent positions on the pristine as well as the $Ru_8$–$NiSe_2$ systems. The calculated values of these free energy changes, along with $\eta$, at various positions on the pristine and $Ru_8$–$NiSe_2$ systems, are compiled in Table S7 (ESI).† From this table we observe that the value of $\Delta G_3$ is maximum at all the possible positions, indicating that the O* → OOH* step is the rate-determining as well as the potential-determining step.

The free energy plots for the OER on pristine and $Ru_8$–$NiSe_2$ surfaces, at the positions where the overpotential is minimum, are presented in Fig. 8. In this figure, we also demonstrate the structural evolution of the various intermediates on the pristine and Ru cluster-decorated surfaces. It is noteworthy that on both the clean and $Ru_8$–$NiSe_2$ (210) surfaces, the OER active sites are the Se-top positions. From Table S7 (ESI)† and Fig. 8, it is clear that the minimum OER overpotential is 0.88 V at one of the Se-top sites on the pristine $NiSe_2$ surface, while this value decreases to 0.79 V after Ru cluster decoration. Due to this reduction in the overpotential value caused by Ru cluster decoration, we expect that $Ru_8$–$NiSe_2$ may serve as a marginally better catalyst for the OER than pure $NiSe_2$.

## Conclusions

In summary, we have demonstrated an energy-efficient and scalable electrosynthesis approach for the synthesis of ruthenium nanocluster decorated nickel diselenide catalysts for high-performance and stable alkaline water splitting application. We optimized the catalyst synthesis, and 50-Ru–$NiSe_2$ was found to exhibit a very low HER overpotential of 13 mV at a current density of 10 mA $cm^{-2}$ and an OER overpotential of 260 mV at a current density of 30 mA $cm^{-2}$. A full cell has been designed using 50-Ru–$NiSe_2$ as both the anode and cathode, which showed a cell potential of 1.45 V to deliver a current density of 10 mA $cm^{-2}$, and we performed a long-term 400 h stability test which showed negligible degradation in current density. The enhancement in the catalytic activity of $NiSe_2$ towards the HER and OER, after Ru cluster decoration, was also investigated *via* density functional theory calculations, and the

 

results of these calculations fully explain the experimental findings. The present work thus provides a new approach to design metal nanocluster-decoration over transition metal selenide-based electrocatalysts, resulting in high electrocatalytic activity, improved electrochemically active sites, and enhanced stability for the alkaline water splitting process.

## Author contributions

V. Y. and M. M. S. conceived the idea and designed the experiments. V. Y. performed all the experiments including synthesis of the catalysts, characterization of the materials, and electrochemical studies. V. Y. and M. M. S. analysed the experimental data. P. S. designed the computational part of the work based on discussions with others. P. S. and M. S. performed the theoretical studies, analysed the computational data, and wrote the portions of the manuscript related to the computational studies. V. Y. wrote the manuscript with inputs from others. M. M. S. and P. S. reviewed and edited the manuscript. M. M. S. supervised all aspects of the experimental work.

## Conflicts of interest

There are no conflicts to declare.

## Acknowledgements

M. M. S. acknowledges the Department of Science & Technology, Govt. of India (DST/TMD/HFC/2k18/136), Science and Engineering Research Board, Department of Science and Technology, India, (CRG/2021/006246), and IISER Thiruvananthapuram, for the financial support. V. Y. is grateful to the Govt. of India, for a PhD scholarship through the Prime Minister's Research Fellowship.

## References

1 J. Zhao, J. J. Zhang, Z. Y. Li and X. H. Bu, *Small*, 2020, **16**, 2003916.
2 M. Ďurovič, J. Hnát and K. Bouzek, *J. Power Sources*, 2021, **493**, 229708.
3 I. Lucentini, X. Garcia, X. Vendrell and J. Llorca, *Ind. Eng. Chem. Res.*, 2021, **60**, 18560–18611.
4 X. Chu, C. I. Sathish, J.-H. Yang, X. Guan, X. Zhang, L. Qiao, K. Domen, S. Wang, A. Vinu and J. Yi, *Small*, 2023, 2302875.
5 C. N. R. Rao and S. Dey, *Proc. Natl. Acad. Sci. U. S. A.*, 2017, **114**, 13385–13393.
6 P. V. Sarma, T. V. Vineesh, R. Kumar, V. Sreepal, R. Prasannachandran, A. K. Singh and M. M. Shaijumon, *ACS Catal.*, 2020, **10**, 6753–6762.
7 Z.-N. Zhang, X.-H. Wang, X.-L. Tian, Y. Chen and S.-N. Li, *J. Mater. Chem. A*, 2023, **11**, 21628–21635.
8 Q. Xue, X.-Y. Bai, Y. Zhao, Y.-N. Li, T.-J. Wang, H.-Y. Sun, F.-M. Li, P. Chen, P. Jin, S.-B. Yin and Y. Chen, *J. Energy Chem.*, 2022, **65**, 94–102.
9 N. P. Dileep, P. V. Sarma, R. Prasannachandran, V. Surendran and M. M. Shaijumon, *ACS Appl. Nano Mater.*, 2021, **4**, 7206–7212.
10 N. P. Dileep, T. V. Vineesh, P. V. Sarma, M. V. Chalil, C. S. Prasad and M. M. Shaijumon, *ACS Appl. Energy Mater.*, 2020, **3**, 1461–1467.
11 P. V. Sarma, T. V. Vineesh, R. Kumar, V. Sreepal, R. Prasannachandran, A. K. Singh and M. M. Shaijumon, *ACS Catal.*, 2020, **10**, 6753–6762.
12 R. Prasannachandran, T. V. Vineesh, M. B. Lithin, R. Nandakishore and M. M. Shaijumon, *Chem. Commun.*, 2020, **56**, 8623–8626.
13 Y. Bai, Y. Wu, X. Zhou, Y. Ye, K. Nie, J. Wang, M. Xie, Z. Zhang, Z. Liu, T. Cheng and C. Gao, *Nat. Commun.*, 2022, **13**, 6094.
14 T. V. Vineesh, U. V. Anagha, N. P. Dileep, H. Cheraparambil, J. Nambeesan and M. M. Shaijumon, *ChemElectroChem*, 2020, **7**, 3319–3323.
15 L. Li, B. Wang, G. Zhang, G. Yang, T. Yang, S. Yang and S. Yang, *Adv. Energy Mater.*, 2020, **10**, 2001600.
16 A. Shan, X. Teng, Y. Zhang, P. Zhang, Y. Xu, C. Liu, H. Li, H. Ye and R. Wang, *Nano Energy*, 2022, **94**, 106913.
17 J. Li, J. Hu, M. Zhang, W. Gou, S. Zhang, Z. Chen, Y. Qu and Y. Ma, *Nat. Commun.*, 2021, **12**, 3502.
18 N. K. Dang, J. N. Tiwari, S. Sultan, A. Meena and K. S. Kim, *Chem. Eng. J.*, 2021, **404**, 126513.
19 P. Thangavel, G. Kim and K. S. Kim, *J. Mater. Chem. A*, 2021, **9**, 14043–14051.
20 B. Kim, T. Kim, K. Lee and J. Li, *ChemElectroChem*, 2020, **7**, 3578–3589.
21 B. M. Leonard, in *Encyclopedia of Inorganic and Bioinorganic Chemistry*, 2021, pp. 1–27.
22 S. Kumaravel, K. Karthick, S. S. Sankar, A. Karmakar, R. Madhu, K. Bera and S. Kundu, *Sustain. Energy Fuels*, 2021, **5**, 6215–6268.
23 F. Song, L. Bai, A. Moysiadou, S. Lee, C. Hu, L. Liardet and X. Hu, *J. Am. Chem. Soc.*, 2018, **140**, 7748–7759.
24 Y. Liu, Y. Guo, Y. Liu, Z. Wei, K. Wang and Z. Shi, *Energy Fuels*, 2023, **37**, 2608–2630.
25 P. V. Sarma, A. Kayal, C. H. Sharma, M. Thalakulam, J. Mitra and M. M. Shaijumon, *ACS Nano*, 2019, **13**, 10448–10455.
26 R. Prasannachandran, T. V. Vineesh, A. Anil, B. M. Krishna and M. M. Shaijumon, *ACS Nano*, 2018, **12**, 11511–11519.
27 Y. Zhao, B. Jin, Y. Zheng, H. Jin, Y. Jiao and S.-Z. Qiao, *Adv. Energy Mater.*, 2018, **8**, 1801926.
28 Z. Zou, X. Wang, J. Huang, Z. Wu and F. Gao, *J. Mater. Chem. A*, 2019, **7**, 2233–2241.
29 D. Damien, A. Anil, D. Chatterjee and M. M. Shaijumon, *J. Mater. Chem. A*, 2017, **5**, 13364–13372.
30 B. Sun, G. Dong, J. Ye, D. Chai, X. Yang, S. Fu, M. Zhao, W. Zhang and J. Li, *Chem. Eng. J.*, 2023, **459**, 141610.
31 M. Singh, T. T. Nguyen, J. Balamurugan, N. H. Kim and J. H. Lee, *Chem. Eng. J.*, 2022, **430**, 132888.
32 M. Ahmad, B. Xi, Y. Gu, H. Zhang and S. Xiong, *Inorg. Chem. Front.*, 2022, **9**, 448–457.
33 Q. Zhao, D. Zhong, L. Liu, D. Li, G. Hao and J. Li, *J. Mater. Chem. A*, 2017, **5**, 14639–14645.

34 K. Chang, D. T. Tran, J. Wang, N. H. Kim and J. H. Lee, *J. Mater. Chem. A*, 2022, **10**, 3102–3111.
35 B. Xu, H. Yang, L. Yuan, Y. Sun, Z. Chen and C. Li, *J. Power Sources*, 2017, **366**, 193–199.
36 Q. Hu, K. Gao, X. Wang, H. Zheng, J. Cao, L. Mi, Q. Huo, H. Yang, J. Liu and C. He, *Nat. Commun.*, 2022, **13**, 3958.
37 M. P. de Lara-Castells, C. Puzzarini, V. Bonačić-Koutecký, M. A. López-Quintela and S. Vajda, *Phys. Chem. Chem. Phys.*, 2023, **25**, 15081–15084.
38 J. Cai, R. Javed, D. Ye, H. Zhao and J. Zhang, *J. Mater. Chem. A*, 2020, **8**, 22467–22487.
39 L. Chen, B. Lu, J. Zhang, R. Wu and Y. Guo, *J. Colloid Interface Sci.*, 2022, **623**, 897–904.
40 H. Hu, F. M. D. Kazim, Q. Zhang, K. Qu, Z. Yang and W. Cai, *ChemCatChem*, 2019, **11**, 4327–4333.
41 J. Zhu, R. Lu, W. Shi, L. Gong, D. Chen, P. Wang, L. Chen, J. Wu, S. Mu and Y. Zhao, *Energy Environ. Mater.*, 2023, **6**, e12318.
42 X. Gu, M. Yu, S. Chen, X. Mu, Z. Xu, W. Shao, J. Zhu, C. Chen, S. Liu and S. Mu, *Nano Energy*, 2022, **102**, 107656.
43 Y. Zheng, Y. Jiao, Y. Zhu, L. H. Li, Y. Han, Y. Chen, M. Jaroniec and S.-Z. Qiao, *J. Am. Chem. Soc.*, 2016, **138**, 16174–16181.
44 J. Yu, Q. He, G. Yang, W. Zhou, Z. Shao and M. Ni, *ACS Catal.*, 2019, **9**, 9973–10011.
45 Q. Hu, K. Gao, X. Wang, H. Zheng, J. Cao, L. Mi, Q. Huo, H. Yang, J. Liu and C. He, *Nat. Commun.*, 2022, **13**, 3958.
46 R. Qin, P. Wang, Z. Li, J. Zhu, F. Cao, H. Xu, Q. Ma, J. Zhang, J. Yu and S. Mu, *Small*, 2022, **18**, 2105305.
47 Z. Pu, Y. Luo, A. M. Asiri and X. Sun, *ACS Appl. Mater. Interfaces*, 2016, **8**, 4718–4723.
48 G. Kresse and J. Hafner, *Phys. Rev. B: Condens. Matter Mater. Phys.*, 1993, **47**, 558–561.
49 G. Kresse and J. Hafner, *Phys. Rev. B: Condens. Matter Mater. Phys.*, 1994, **49**, 14251–14269.
50 G. Kresse and J. Furthmüller, *Comput. Mater. Sci.*, 1996, **6**, 15–50.
51 G. Kresse and J. Furthmüller, *Phys. Rev. B: Condens. Matter Mater. Phys.*, 1996, **54**, 11169–11186.
52 J. P. Perdew, K. Burke and M. Ernzerhof, *Phys. Rev. Lett.*, 1996, **77**, 3865–3868.
53 P. E. Blöchl, *Phys. Rev. B: Condens. Matter Mater. Phys.*, 1994, **50**, 17953–17979.
54 S. Grimme, J. Antony, S. Ehrlich and H. Krieg, *J. Chem. Phys.*, 2010, **132**, 154104.
55 X. Hu, X. Tian, Y.-W. Lin and Z. Wang, *RSC Adv.*, 2019, **9**, 31563–31571.
56 C. Gu, S. Hu, X. Zheng, M.-R. Gao, Y.-R. Zheng, L. Shi, Q. Gao, X. Zheng, W. Chu, H.-B. Yao, J. Zhu and S.-H. Yu, *Angew. Chem., Int. Ed.*, 2018, **57**, 4020–4024.
57 S. K. Ramesh, V. Ganesan and J. Kim, *ACS Appl. Energy Mater.*, 2021, **4**, 12998–13005.
58 H. Huang, Y. Zhao, Y. Bai, F. Li, Y. Zhang and Y. Chen, *Adv. Sci.*, 2020, **7**, 2000012.
59 B. Xu, H. Yang, L. Yuan, Y. Sun, Z. Chen and C. Li, *J. Power Sources*, 2017, **366**, 193–199.
60 Z. Zou, X. Wang, J. Huang, Z. Wu and F. Gao, *J. Mater. Chem. A*, 2019, **7**, 2233–2241.
61 H. Wang, X. Li, Q. Ruan and J. Tang, *Nanoscale*, 2020, **12**, 12329–12335.
62 K. Fan, H. Chen, Y. Ji, H. Huang, P. M. Claesson, Q. Daniel, B. Philippe, H. Rensmo, F. Li, Y. Luo and L. Sun, *Nat. Commun.*, 2016, **7**, 11981.
63 B. Xu, H. Yang, L. Yuan, Y. Sun, Z. Chen and C. Li, *J. Power Sources*, 2017, **366**, 193–199.
64 I. S. Kwon, T. T. Debela, I. H. Kwak, Y. C. Park, J. Seo, J. Y. Shim, S. J. Yoo, J. G. Kim, J. Park and H. S. Kang, *Small*, 2020, **16**, 2000081.
65 J. Zhu, L. Hu, P. Zhao, L. Y. S. Lee and K. Y. Wong, *Chem. Rev.*, 2020, **120**, 851–918.
66 X. Luo, X. Tan, P. Ji, L. Chen, J. Yu and S. Mu, *EnergyChem*, 2023, **5**, 100091.
67 S. Anantharaj and S. Noda, *Int. J. Hydrogen Energy*, 2020, **45**, 15763–15784.
68 I. Demiroglu, K. Yao, H. A. Hussein and R. L. Johnston, *J. Phys. Chem. C*, 2017, **121**, 10773–10780.
69 A. S. Chaves, M. J. Piotrowski and J. L. F. Da Silva, *Phys. Chem. Chem. Phys.*, 2017, **19**, 15484–15502.
70 Y. Wu, L. Wang, T. Bo, Z. Chai, J. K. Gibson and W. Shi, *Adv. Funct. Mater.*, 2023, **33**, 2214375.
71 J. K. Noerskov, T. Bligaard, A. Logadottir, J. R. Kitchin, J. G. Chen, S. Pandelov and U. Stimming, *ChemInform*, 2005, **152**, J23–J26.
72 B. Hinnemann, P. G. Moses, J. Bonde, K. P. Jørgensen, J. H. Nielsen, S. Horch, I. Chorkendorff and J. K. Nørskov, *J. Am. Chem. Soc.*, 2005, **127**, 5308–5309.
73 I. T. McCrum and M. T. M. Koper, *Nat. Energy*, 2020, **5**, 891–899.

 